PHYSICAL REVIEW B VOLUME 57, NUMBER 4 15 JANUARY 1998-II

High coercivity in ultrathin epitaxial micrometer-sized particles with in-plane magnetization: Experiment and numerical simulation

O. Fruchart, J.-P. Nozières, B. Kevorkian, J.-C. Toussaint, and D. Givord
Laboratoire L. Néel, 38042 Grenoble, France

F. Rousseaux, D. Decanini, and F. Carcenac
Laboratoire de Microstructures et Microlectronique (L2M), 92225 Bagneux, France

(Received 28 February 1997)

Arrays of 2.5×10^7 ultrathin epitaxial W(110)/Fe(110)/W(110) submicron particles with in-plane magnetization were fabricated using x-ray lithography and dry-etching techniques. A large coercive-field increase as compared to continuous films is observed which is ascribed to the short range of self-demagnetizing fields for ultrathin particles with in-plane magnetization. A method to extract the mean hysteresis loop of a single particle and the coercive field distribution function from measurements over the whole array is proposed. The analysis is in good agreement with the picture of single-domain particles and of nucleation volumes much smaller than particle dimensions. It is corroborated by micromagnetic calculations performed on isolated ideally square particles. [S0163-1829(98)07804-7]

I. INTRODUCTION

Magnetization reversal understanding in thin and ultrathin films is of considerable interest both for fundamental research and for applications to storage media. In continuous films the magnetization reversal is often governed by extrinsic phenomena such as nucleation at local defects, so that global reversal loops do not reflect the material intrinsic properties. Recent results have shown that it is possible to reduce the influence of these extrinsic sources of reversal by patterning the film into micrometer-sized isolated particles.[1] Most of the corresponding studies reported so far dealt with perpendicular magnetization systems. In this paper, the magnetization reversal in patterned epitaxial ultrathin W(110)/Fe(110)/W(110) films is examined. These systems offer several simplifying advantages for studying magnetization reversal mechanisms: (i) the magnetization vector is uniform throughout the thickness of the film so that only two-dimensional magnetic configurations are involved; (ii) the magnetization is maintained in-plane for all thicknesses,[2] which favors single domain states; and (iii) self-demagnetizing fields are weak because particles are very flat.

II. SAMPLE PREPARATION

The results presented here were obtained on a 60-Å-thick epitaxial Fe film sandwiched between two epitaxial 500-Å buffer and protective W layers. The growth was performed under UHV conditions using pulsed-laser-deposition. Details about preparation conditions were given elsewhere.[3] The submicron patterning was achieved using x-ray lithography, implemented at the L2M facility at the super-ACO storage ring in Lure, France. X-ray lithography presents several specific advantages with respect to other lithography techniques: (i) the short wavelength of x rays allows high resolution (<1000 Å) and high aspect ratios to be achieved, (ii) due to diffraction limited phenomena the mask-to-sample distance is not so critical as for optical or uv lithography, and (iii) the replication time is short (typically 1 min) and does not depend upon the sample area.

The replication masks realized at the L2M laboratory consist of an x-ray transparent silicon carbide (SiC) membrane supporting x-ray-absorbant tungsten (W) or gold (Au) structures.[4] Mask patterns are defined by a vector scan nanopattern generator working at 50-keV energy. Using a lift-off process with Ni, the patterns are transferred in W by reactive ion etching. In the case of gold absorber, gold features are grown by an electroplating process. Special care was needed to realize large patterned areas on the mask (up to $5\times5\,\mathrm{mm}^2$) in order to allow macroscopic magnetic measurements.[5] In the present case x-ray lithography was performed in a close proximity with a mask-to-wafer distance of 40 μm using an x-ray stepper. The different steps involved in the sample patterning are summarized in the scheme of Fig. 1(a). X-ray exposures were done on a high sensitivity negative resist SAL601 (Shipley), resulting in arrays of holes as shown in Fig. 1(b). The resist duplication was followed by a lift-off with aluminum (400 Å) resulting in an array of Al patterns [Fig. 1(c)]. The film was then etched using successively SF_6/CHF_3 RIE to increase the mask aspect ratio by duplicating it into the W protective layer, and Ar-ion-beam-etching (IBE) to etch the Fe layer. A 1500-Å Cu capping layer was *in situ* evaporated to prevent oxidation of the Fe particles edges [Fig. 1(d)]. Such a protection appears to be essential as recent measurements on isolated particles have shown dramatic dependence of nucleation processes on particles surface oxidation.[6]

The sample examined in the present study consists of a $5\times5\text{-mm}^2$ array of square particles with 0.5-μm edges separated by 1 μm. The edges of the particles are parallel to the in-plane magnetic axes of the film, i.e., [001] and $[1\bar{1}0]$ (Fig. 1).

III. MAGNETIC MEASUREMENTS OVER THE WHOLE ARRAY

For W/Fe/W continuous films (referred in the following as cf) it was shown in Ref. 2 that the magnetization remains

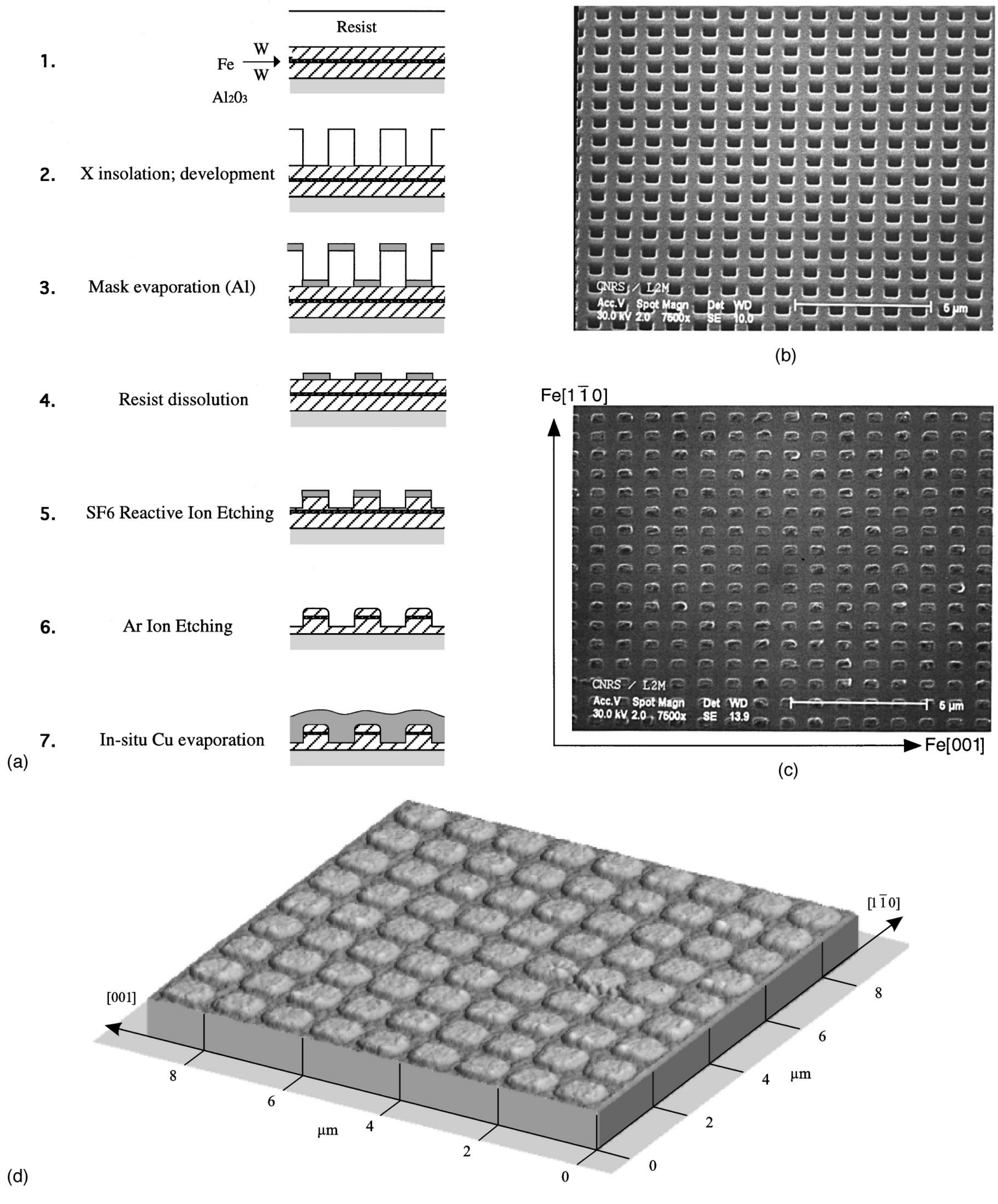

FIG. 1. The lithographic preparation process (a). Scanning-electron-microscopy pictures in (b) and (c) show, respectively, the revealed resist (step 2) and the lifted-off Al (step 4). Particles covered by the *in situ* evaporated 1500-Å-thick Cu layer were imaged *ex situ* using contact-mode AFM (step 7) (d).

in plane whatever the thickness. This is because the interface anisotropy favors in-plane magnetization and thus reinforces shape anisotropy. It is found in addition that the in-plane magnetization easy-axis changes as the film thickness is reduced: above 100-Å bulk anisotropy sources (magnetocrystalline and magnetoelastic) dominate, and the easy axis lies along the in-plane $[001]$ axis, as in bulk Fe. Below 50 Å the interface anisotropy overcomes the bulk anisotropy, and the easy axis is along the in-plane $[1\bar{1}0]$ axis (Fig. 2). Between 50 and 100 Å, interface and bulk anisotropy contributions nearly compensate for each other. Because of differences in their temperature dependences, the easy axis direction varies with temperature: for the 60-Å-thick sample presented here, $[1\bar{1}0]$ is the easy axis and $[001]$ a hard axis at 300 K, while at 10 K both axes show a similar easy-axis-like behavior (Fig. 2). This interesting property allows us to vary the anisotropy field in the same film just by changing temperature. A detailed discussion of this temperature-driven transition can be found elsewhere.[3]

Magnetization loops of the array of particles measured with a custom high sensitivity vibrating sample magnetometer (VSM) at different temperatures are shown in Fig. 2. In

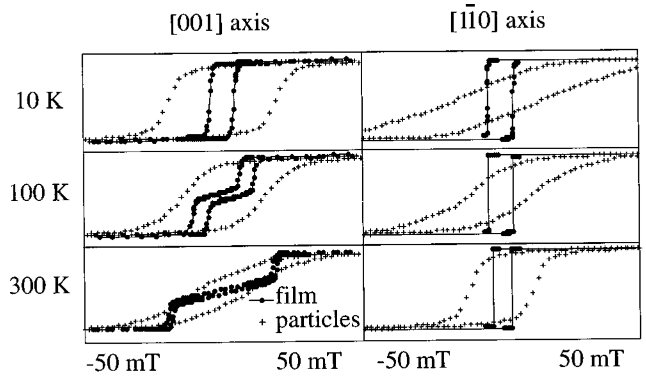

FIG. 2. Superimposed normalized in-plane hysteresis loops of the same W(110)500 Å/Fe(110)60 Å/W(110)500 Å sample, as a continuous film (●) and as an array of particles (+).

this figure, the data were renormalized and superimposed on the continuous film loops for comparison. The patterned film differs from the continuous one in three aspects: (i) the coercive field is increased, especially for easy-axis-like loops (see [001] at 10 K for example); (ii) the reversal is broadened and an earlier departure from saturation occurs; and (iii) an irreversible contribution to hard-axis loops is observed.

In order to interpret these results one needs first to determine whether particles behave independently or whether interparticule dipolar interactions play a dominant role in magnetization reversal. Stray fields generated by a uniformly magnetized particle on its neighbors were calculated, using the surface poles analogy. Calculation is simplified in the limit of ultrathin particles, i.e., when the ratio of particle thickness over interparticle spacing $\epsilon = t/L$ is much smaller than unity (in the present case, $\epsilon = 0.012$). The center of the uniformly magnetized particle was used as origin.

$\alpha = x/L$ and $\beta = y/L$ are the in-plane reduced coordinates. When the magnetization m lies along y, the stray field on the surrounding particles can be expressed as

$$\mu_0 h_x(\alpha,\beta) = \frac{\epsilon\mu_0 m}{4\pi} \sum_{\substack{\delta_1=\pm1\\ \delta_2=\pm1}} \frac{\delta_1\delta_2}{\sqrt{\left(\alpha-\frac{\delta_1}{2}\right)^2+\left(\beta-\frac{\delta_2}{2}\right)^2}}, \tag{1}$$

$$\mu_0 h_y(\alpha,\beta) = -\frac{\epsilon\mu_0 m}{4\pi} \sum_{\substack{\delta_1=\pm1\\ \delta_2=\pm1}} \frac{\delta_1\delta_2}{\sqrt{\left(\alpha-\frac{\delta_1}{2}\right)^2+\left(\beta-\frac{\delta_2}{2}\right)^2}} \times \frac{\alpha-\frac{\delta_1}{2}}{\beta-\frac{\delta_2}{2}}. \tag{2}$$

An upper bound to the total stray field acting on a given particle and originating in surrounding particles is obtained by assuming that all contributions add up in absolute values, i.e., as if the directions of magnetization of these particles (along $+y$ or $-y$) were taken such that all contributions were of the same sign (full symbols in Fig. 3). The resulting contribution coming from nearest neighbors is less than 2 mT. Farther particles can be viewed as localized dipoles, generating a $1/r^3$ stray field. As all particles lie on a two-dimensional (2D) array, the overall stray field is bounded by a series with $2\pi r/r^3 \sim 1/r^2$ terms. This series converges with a $1/r$ error, which means that dipole-dipole interactions are short ranged in our system. This can be understood as the stray fields generated by particles expand into a 3D space, whereas the magnetic material is confined to a 2D space: the resulting magnetostatic energy is small. Generally the magnetic material shape is 3D and the magnetostatic energy is large, resulting in a long-range dipole-dipole interaction. In our case it is found numerically that convergence is achieved with second or third neighbors, resulting in total fields which never exceed 3 mT (Fig. 3). Such fields will be neglected to first approximation, given the values of experimental coercive fields (>15 mT). One might object that the magnetization distribution in real particles may not be homogeneous, showing flower or even multidomain configurations.[7] Long-distance stray fields for such configurations will, however, be smaller than for uniformly magnetized single-domain states, so that the stray fields calculated above represent an upper bound for experimental stray fields.

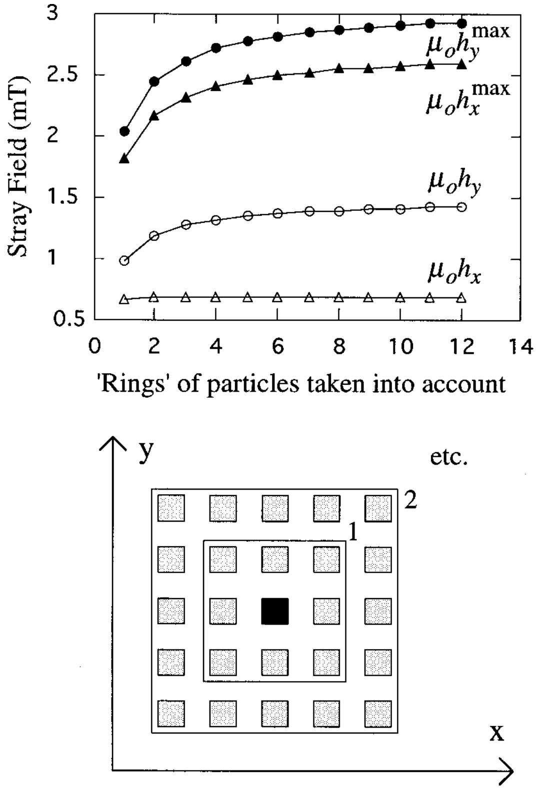

FIG. 3. Calculated stray fields along x and y in the angle of a particle, created by surrounding particles uniformly magnetized along the y axis. Contributions have been summed for particles included in concentric squares. Contributions have been added algebraically (open symbols) and in absolute values for an estimation of the highest possible stray field (full symbols).

The increase of the mean coercive field in patterned films with respect to the continuous film is clearly illustrated by

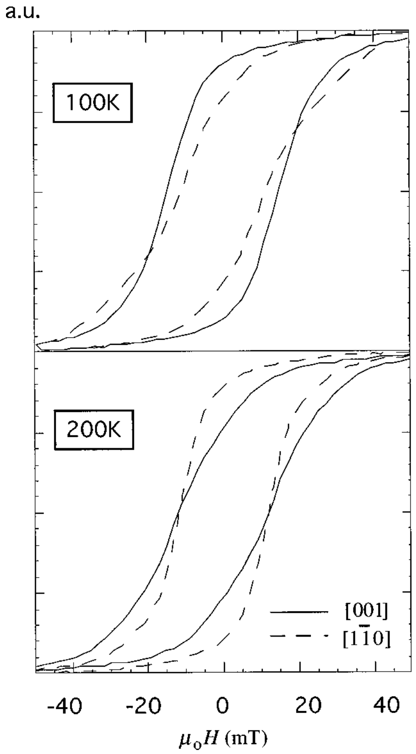

FIG. 4. The in-plane reorientation transition in the patterned film is found to be around 150 K.

comparing respective hysteresis loops. This is done in Fig. 2 for H parallel to [001] and $[1\bar{1}0]$, respectively. In order to analyze these hysteresis loops, phenomenological anisotropy constants must be determined. For the continuous film the experimental hard-axis loops could be well fitted using the phenomenological in-plane anisotropy energy

$$E_a = A_{cf}\sin^2(\varphi) + B_{cf}\sin^4(\varphi), \tag{3}$$

where φ is the angle between [001] and the magnetization direction.[8] Unfortunately the anisotropy has been modified by the patterning: the $[1\bar{1}0]$ axis tends to be ‘‘less an easy axis’’ for the particles than for the continuous film (Fig. 2; see, for instance, $[1\bar{1}0]$ at 10 K). This modification could be the consequence of the strain being different in the continuous film and in the patterned film. The anisotropy modification could also be due to the fact that the particle edges are associated with an interface anisotropy, which originates in the symmetry breaking of local environments of Fe atoms in contact with evaporated Cu atoms. However, both systems (particles and continuous film) show the same type of anisotropy variation with temperature: magnetization alignment along $[1\bar{1}0]$ is favored at room temperature whereas [001] tends to become the easy axis of magnetization when the temperature is decreased. The transition temperature is near 0 K for the continuous film, and just above 150 K (Fig. 4) for the array (see also Ref. 3 for the cf analysis). As A_{cf} and B_{cf} vary nearly linearly with temperature between 10 and 300 K, we made the simplifying assumption that the values of the anisotropy constants of the particles at 300 K, $A_p(T=300\text{ K})$ and $B_p(T=300\text{ K})$, are equal to the values of the anisotropy constants of the continuous film at 150 K, $A_{cf}(T=150\text{ K})$ and $B_{cf}(T=150\text{ K})$. This assumption is supported by the fact that the relatively small anisotropy values in the present system result from the near cancellation of larger anisotropy sources opposite in sign (magnetocristalline/magnetoelastic, and interface),[3] so that the large relative change of the total anisotropy observed in our system comes from small relative changes in the different contributions to the total anisotropy. The thermal variations of the involved anisotropy constants (not to be confused with temperature- and system-dependent coercive fields) depend on band structures, which are not expected to be much different in particles than in a continuous film. We therefore expect the thermal variation of the anisotropy constants to be nearly the same in particles than in a continuous film. It is also interesting to note that although the total anisotropy constants A_{cf} and B_{cf} in the continuous film vary significantly between 100 and 300 K (see Fig. 5), the coherent-rotation Stoner-Wohlfarth (SW) field along the $[1\bar{1}0]$ axis $\mu_0 h_{SW} = (2A_{cf} + 4B_{cf})/M_s$ remains almost unchanged ($\mu_0 h_{SW} \approx 550$ Oe) because the thermal variations in A_{cf} and B_{cf} tend to cancel each other. We stress that the assumption made above may perhaps lead to only semi-quantitative results.

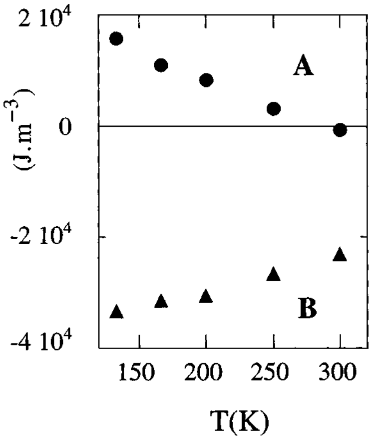

FIG. 5. In-plane-anisotropy second-order constant A_{cf} and fourth-order constant B_{cf} as deduced from the hard-axis cycle on the continuous film. $A_{cf} \approx B_{cf}$ can be extrapolated at 10 K, which explains why both axis show an easylike behavior at low temperature (Fig. 2).

According to the above discussion we analyzed the respective reversal properties of the continuous film at 150 K and of the particles at 300 K. In-plane anisotropy energy profiles can be drawn at the coercive fields of the film ($\mu_0 h_{cf} = -4$ mT at 150 K) and at that of the array of particles ($\mu_0 h_p = -14$ mT at 300 K) (Fig. 6). It can be seen that starting from saturation along the $[1\bar{1}0]$ direction, the magnetization in the continuous film reverses when the absolute energy minimum for the final state ($[\bar{1}10]$ direction) is only slightly lower than for the initial state ($[1\bar{1}0]$ direction), i.e., the magnetization reverses almost as soon as one state becomes energetically favored compared to the other. The picture is very different in a particle, where it is found that at the reversal field, the energy minimum in the $[\bar{1}10]$ direction is far deeper than in the $[1\bar{1}0]$ direction, i.e., the initial state has already become highly metastable against the final state. This difference can be analyzed in the framework of

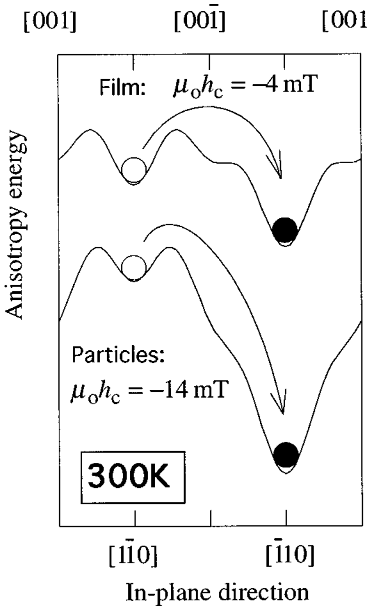

FIG. 6. Calculated anisotropy free-energy profile as a function of the in-plane magnetization direction, at 300 K, for the continuous film (top) and an isolated particle (bottom). The profile is drawn for the respective experimental mean coercive fields, using the phenomenological anisotropy constants A_{cf} and B_{cf} from Fig. 4.

the nucleation-expansion-propagation model:[9] the magnetization reversal is described as a three-stage process: (i) the nucleation of a reversed domain (generally located at anisotropy and/or surface defects); (ii) a reversible quasistatic expansion of that domain, up to a critical size; and (iii) the explosion of the reversed domain through the whole material via propagation of a domain wall. The coercive field is the maximum value between the propagation field and the lowest nucleation-expansion field in the sample. Ideal in-plane magnetization Fe epitaxial films have no pinning sites, so that the magnetization reversal is expected to be governed by the lowest existing nucleation-expansion field. The presence of numerous defects throughout the film (scratches, irregular edges, etc.) may considerably lower the nucleation-expansion field, and thus the coercive field, as compared to the anisotropy field. However, an isolated defect, which would reverse the whole sample in a continuous film, affects only a single particle in an array (at least as long as the particle density is much larger than the mean defect density).

In the classical theory of magnetization reversal it is assumed that in an ideal system where local defects can be neglected, coherent rotation of the magnetization occurs. This is the well-known Stoner-Wohlfarth (SW) model.[10] Actually, nonuniform magnetization configurations may appear in order to minimize the self-dipolar energy, thus lowering the reversal field as compared to the coherent rotation field. In the case of ultrathin particles with in-plane magnetization, the surface poles are located on a nearly one-dimensional surface (the edges of the particle). These poles therefore have a limited influence on the two-dimensional nucleation volume, and the single-domain state is the most stable one. That this is true was actually confirmed experimentally by magnetic force microscopy (MFM) imaging on W/Fe/W particles prepared by New *et al.*[11] Highly metastable states may thus be obtained, resulting in high coercive fields. The experimental coercive field may in principle reach the SW coherent rotation value when the film thickness reduces toward zero. It may, however, be difficult to obtain $h \rightarrow h_{\mathrm{SW}}$ experimentally, as the SW energy barrier $\Delta e(h)$ to be overcome during reversal varies more rapidly than $h - h_{\mathrm{SW}}$: $\Delta e(h) \sim (h - h_{\mathrm{SW}})^k$, with k ranging from $2(h \rightarrow h_{\mathrm{SW}})$ to more than 4 at small field. Moreover the above simple picture of a particle located in a two-well energy profile is valid only for a system characterized by a single degree of freedom. In reality, the energy of the nucleation volume may be obtained by a complex weighted integration over a large range of spin angle, due to the nonuniform configurations of the nucleation volume (in particular because spins tend to align along the neighboring edges of the particle). The combined effect of reducing the barrier height and the angle extension of the local minimum of the energy profile may be viewed as leading to an effective barrier varying much more rapidly with h than Δe, thus considerably lowering h_c as compared to h_{SW}.

It is worth noting that the picture is very different in the case of in-plane anisotropy for nonultrathin particles, or for perpendicular anisotropy particles for which the surface poles are located on a two-dimensional surface. The influence of these poles is dominant in the nucleation process: multidomain states may appear, and the reversal behavior is not very different from that of the continuous film[1] as long as the particle size is well above the domain-wall width.[12] Note that the criterion for an in-plane anisotropy particle to be considered as 2D is $t/\lambda_n \ll 1$, where t is the film thickness and λ_n the Neél wall width. The demagnetizing field due to surface poles is then non-negligible over a small fraction only of the nucleation volume, and the mean demagnetizing energy in this nucleation volume is small. In the present case $\lambda_n \sim 1000$ Å, so that the condition $t/\lambda_n \ll 1$ is well fulfilled.

IV. SINGLE-PARTICLE REVERSAL-DECONVOLUTION MODEL

The description of the exact reversal mechanism from the global magnetization reversal of a 2.5×10^7-particle array is complex due to statistical differences between particles. Assemblies of magnetically coupled particles are commonly studied in the framework of Preisach models.[13] If some statistical knowledge about both the irreversible and reversible contributions to individual particle reversal loops is desired, one has to use the nonlinear Preisach model, whose resolution requires a two-dimensional set of experimental curves (i.e., a three-dimensional set of data), which is experimentally time consuming. Moreover, Preisach models were introduced to fit the behavior of an assembly of strongly interacting particles. In the case of weakly interacting or noninteracting particles, as is the case here, the statistical study of the system may be considerably simplified. Also, even a detailed resolution of the nonlinear Preisach model would lead to incomplete information about the statistical distribution of the reversible contribution to the hysteresis loops of particles characterized by different values of coercive fields (see Ref. 13, p. 86). The hypothesis made in the simpler method presented in the following proves to be not too restricting as compared to the Preisach model.

We managed to reconstruct the mean reversal loop of a single particle when the magnetic field is applied along the material easy axis. The method is based on the separation of the global loop into reversible and irreversible contributions. The following hypotheses are made: (i) as previously discussed, interparticle dipolar coupling is neglected. (ii) Particles remain single domain for any applied magnetic field. Consequently the hysteresis loop of a single particle can be decomposed into the following multistage process: at first a reversible magnetization variation occurs (given that the field is applied along the easy axis of the particles, this can only be due to nonuniform magnetization configurations, such as field-dependent flower states[7]). Then, at h_c, an irreversible reversal occurs, that is characterized by a magnetization jump Δm. Finally a progressive and reversible alignment of the magnetization along the field takes place. (iii) To first approximation, it is assumed that the reversible contribution to the total magnetization reversal in a single particle is the same function, called m_r, for all particles. The question arises of whether the argument of this function should be h or $\tilde{h}=h-h_c$. $m_r(h)$ would describe systems where the reversible and irreversible magnetization variations take place independently. This is the case in most materials where the irreversible magnetization reversal is triggered by the nucleation at local defects, whereas the reversible magnetization variation involves all the moments. $m_r(\tilde{h})$ corresponds to the case where the reversible magnetization variation before the reversal reflects a nucleation process that will trigger the irreversible jump. This description is justified for defect-free systems, as is expected to be the case here. To verify this hypothesis the analysis described below was tentatively performed with h as an argument for m_r, and the results obtained appeared to be unphysical.

The assembly of particles is eventually characterized by two functions only: the coercive field distribution function $\rho(h)$ and the reversible contribution to the reversal $m_r(\tilde{h})$. This can be respectively summarized for a single particle and for the array in the formulas

$$\left.\frac{dm}{dh}(h)\right|_{\text{single}} = \Delta m\,\delta(h-h_c) + \frac{dm_r}{dh}(h-h_c), \qquad (4)$$

$$\left.\frac{dm}{dh}(h)\right|_{\text{array}} = \Delta m\,\rho(h) + \int \rho(h_c)\frac{dm_r}{dh}(h-h_c)\,dh_c. \qquad (5)$$

The two experimental functions used to solve Eqs. (4) and (5) for $\rho(h)$ and $m_r(\tilde{h})$ are the total magnetization decrease $(dm/dh)(h)|_{\text{tot}}^{\text{expt}}$ and the dc reversible susceptibility $\chi(h)|_{\text{dc}}^{\text{expt}}$.

These two experimental functions are respectively identified in Eq. (5) to the total term $(dm/dh)(h)|_{\text{array}}$ and the reversible term $\int\rho(h_c)(dm_r/dh)(h-h_c)dh_c$, yielding

$$\rho(h) = \frac{1}{\Delta m}\left[\left.\frac{dm}{dh}(h)\right|_{\text{tot}}^{\text{expt}} - \left.\chi(h)\right|_{\text{dc}}^{\text{expt}}\right]. \qquad (6)$$

$m_r(h)$ is then obtained by deconvolution using fast Fourier transform (FFT)

$$m_r(h) = \int_{-\infty}^{h} \mathcal{F}\left[\frac{\mathcal{F}(\chi_{\text{dc}}^{\text{expt}})}{\mathcal{F}(\rho)}\right]. \qquad (7)$$

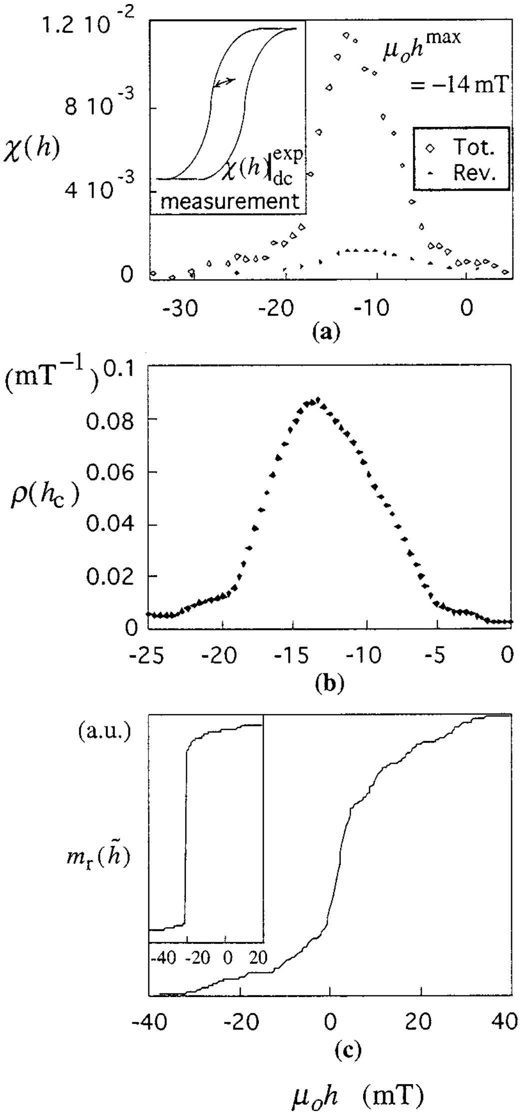

FIG. 7. Experimental data used for the deconvolution model (a) and the corresponding outputs of the model: $\rho(h_c)$ (b) and $m_r(\tilde{h})$ (c). The inset in (c) displays the reconstructed mean reversal loop of a single particle. The high irreversible contribution (reversible contribution) ratio justifies the single-domain hypothesis used in the model.

Experimental $(dm/dh)(h)|_{\text{tot}}^{\text{expt}}$ and $\chi(h)|_{\text{dc}}^{\text{expt}}$ curves along $[1\,\bar{1}\,0]$ at 300 K are shown in Fig. 7(a). $\chi(h)|_{\text{dc}}^{\text{expt}}$ was measured performing a reversible backward minor cycle containing no irreversible contribution [see the insert in Fig. 7(a)]. $\rho(h)$ and $m_r(\tilde{h})$ are reported in Figs. 7(b) and 7(c).

The above deconvolution procedure yields very sound outputs which give credit to the model: (i) the main contribution to the magnetization reversal of the array of particles is irreversible (80%), which would not be the case for multidomain particles; (ii) the $m_r(\tilde{h})$ function shows an angular point for $\tilde{h}=0$, which is consistent with the picture of a three-stage nucleation-jump-saturation reversal; and (iii) the reversible deviation from saturation is larger before the irreversible jump than after. Indeed, this is consistent with the discussion about the deviation from saturation in Sec. II (see Fig. 6): at h_c the anisotropy energy well along the $[\bar{1}10]$

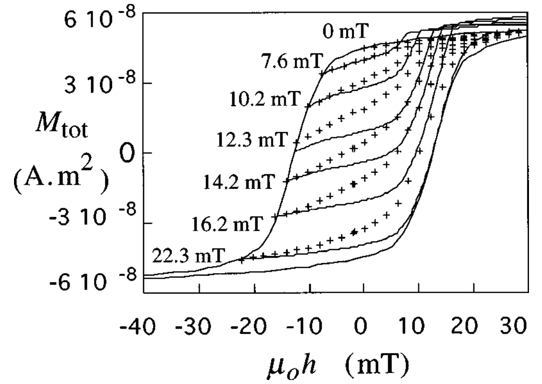

FIG. 8. Experimental (+) and simulated (−) minor loops. The discrepancy may be ascribed to a small amount of in-plane 70° twinned crystallites.

direction (final state) is much deeper than in the $[1\,\overline{1}\,0]$ direction (initial state), so that the free-energy minimization will favor more aligned configurations after the reversal than before.

The validity of the model can be further tested by comparing simulated and experimental minor loops at different stages of the reversal in the array: after positive saturation $(h=+\infty)$, the field is reduced to a negative field h_0 and increased again $(h=+\infty)$. When increasing the field from h_0, unreversed (up) particles (for which $h_c<h_0$) and reversed (down) particles (for which $h_0<h_c$) have to be taken into account separately in the simulation. According to the time-reversal symmetry a down particle is characterized by a $\rho(-h)$ coercive field distribution and a $(dm_r/dh)(-\tilde{h})$ reversible contribution. The change of magnetization during the minor cycle can accordingly be written

$$\left.\frac{dm}{dh}(h)\right|_{\text{array}}=\int_{-\infty}^{h_0}\rho(h_c)\frac{dm_r}{dh}(h-h_c)dh_c+\int_{h_0}^{+\infty}\rho(-h_c)\frac{dm_r}{dh}\times(-h-h_c)dh_c \tag{8}$$

$$-\Delta m\rho(-h)H_e(-h-h_0), \tag{9}$$

where H_e is the Heaviside function $[H_e(x)=0$ when $x<0$ and 1 when $x>0]$. Experimental and simulated minor loops for different h_0 fields are superimposed in Fig. 8. The agreement is satisfactory. The discrepancy between experimental and simulated minor loops might be the consequence of a small amount of growth-induced in-plane 70°-twinned crystallites[14] in the film.

Let us now discuss the physical meaning of the $\rho(h)$ function yielded by the analysis. The total half-width at half maximum of $\rho(h)$ amounts to 8 mT. As discussed in Sec. II, interparticule dipolar coupling may account for approximately 2 mT in the field distribution of $\rho(h_c)$. A fraction of the coercive field distribution may also be ascribed to sample thickness inhomogeneities: the SW reversal-field reduction due to the adjunction of a single Fe monolayer is $(2/n)\times(2A_s/\mu_0M_st)=-6$ mT. A_s is the interface contribution to the second-order anisotropy constant A,n is the number of Fe monolayers of the film, and t is the film thickness. The surface roughness was estimated to about 1.5 ML by analyzing the hard axis reorientation field distribution for the continuous film. As $h_c\simeq0.25h_{\text{SW}}$, this would finally lead to a coercive field distribution of about 2 mT. These two contributions add up to 4 mT at the most; they are insufficient to fully account for the observed 8-mT distribution. Other potential sources for the nucleation field distribution between particles could be patterning-process-induced defects and/or a small amount $(\simeq5\%)$ of twinned crystallites.

Eventually the mean hysteresis loop of a single particle was obtained from $m_r(\tilde{h})$ and the numerical value of Δm provided by the numerical deconvolution analysis [the inset in Fig. 7(c)]. This individual particle mean reversal loop turns out to be very similar to that directly measured with the micro-superconducting-quantum-interference-device technique for a single isolated Co particle.[15]

V. NUMERICAL CALCULATIONS

In this section, we describe the calculation of magnetization reversal in an in-plane magnetization ultrathin particle, and compare the results of numerical calculation to experimental ones. In the continuous medium approximation, the Gibbs free-energy density $F\{\mathbf{m}(\mathbf{r})\}$ of a ferromagnetic system of magnetization vector $\mathbf{M}(\mathbf{r})=M_s\cdot\mathbf{m}(\mathbf{r})$ can be written as

$$F\{\mathbf{m}(\mathbf{r})\}=\int_V d\mathbf{r}(\mathbf{A}\cdot[\mathbf{m}(\mathbf{r})]^2-\mathbf{P}_{\mathbf{K}}[\mathbf{u}_{\mathbf{k}}\cdot\mathbf{m}(\mathbf{r})] \tag{10}$$

$$-\mu_0M_s\mathbf{H}_{\text{ext}}\cdot\mathbf{m}(\mathbf{r})-\tfrac{1}{2}\mu_0M_s\mathbf{m}(\mathbf{r})\cdot\mathbf{H}_{\text{S}}\{\mathbf{m}(\mathbf{r})\}), \tag{11}$$

where $\mathbf{u}_{\mathbf{k}}$ is an anisotropy direction and P_K is a polynome expliciting the magnetocristalline anisotropy energy. $\mathbf{H}_{\text{S}}\{\mathbf{m}(\mathbf{r})\}$ is the stray field due to the magnetostatic volume charges $\rho_m=-M_s(\nabla\cdot\mathbf{m}(\mathbf{r}))$ and surface charges $\sigma_m=M_s\cdot\mathbf{m}(\mathbf{r})\cdot\mathbf{n}$ ($\mathbf{n}$ is the surface normal, pointing outwards). $\mathbf{H}_{\text{S}}$ is derived from a scalar potential ϕ such that

$$\nabla^2\phi_{\text{in}}=\rho_m, \tag{12}$$

$$\nabla^2\phi_{\text{out}}=0, \tag{13}$$

respectively, inside the material (Poisson equation) and outside the material (Laplace equation). This set of partial differential equations has to be solved with ϕ meeting boundary conditions at the material surface

$$\phi_{\text{in}}=\phi_{\text{out}}, \tag{14}$$

$$(\nabla\phi_{\text{in}}-\nabla\phi_{\text{out}})\cdot\mathbf{n}=\sigma_m, \tag{15}$$

and the Dirichlet condition $\phi_{\text{out}}=0$ at infinity. We used the finite-difference method to calculate the potential ϕ associated with a given magnetization distribution $\mathbf{m}(\mathbf{r})$. The values of ϕ and $\mathbf{m}(\mathbf{r})$ were sampled at the cell centers of a regular parallelepipedic mesh with grid spacing (a_x,a_y,a_z).

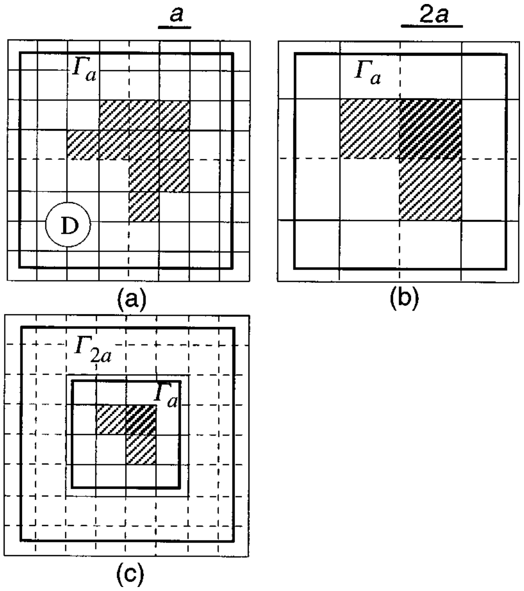

FIG. 9. Scaling transformation of a 2D mesh with a factor $b = 2$. The dashed squares correspond to the magnetized system to be simulated.

The value of ρ_{m} on each node was evaluated using a second-order interpolation of the vector field between the cell and its first neighbors.

In order to obtain an accurate estimate of ϕ, the grid should be extended over a large region outside the magnetized system, which increases computer time. In order to lower this time we developed an iterative renormalization method, allowing, in principle, the projection of the grid outer limit to infinity. Consider for example a 2D bounded square domain D in which the physical system is enclosed, and placed into a square mesh with parameter a. Let us note Γ_a the line joining the set of the outer nodes [Fig. 9(a)]. We apply a scaling transformation defined by a factor b [$b=2$ in Fig. 9(a)] so as to obtain a coarser mesh with parameter ba [Fig. 9(b)]. In each of the new cells the magnetization vector is determined as a vectorial average over the underlying initial cells. A contraction of the grid with the same factor b is then performed [Fig. 9(c)]. The outer line Γ_{ba} after renormalization is farther from the magnetized system than Γ_a was before renormalization. The Poisson equation is then solved while imposing $\phi_{ba}=0$ on Γ_{ba} in the fine mesh of Fig. 9(c), leading to a first set of approximated values for ϕ_{ba}. ϕ_a on Γ_a is then obtained by a linear interpolation of ϕ_{ba}. The system is finally reexpanded to its initial size, and a first approximation of the magnetization configuration is obtained. This renormalization procedure may be further iterated. However the accuracy of the set of ϕ_a cannot be indefinitely improved, because at each step some information on the magnetized system is lost due to the grid coarsening. The method illustrated here for a 2D system may be equivalently applied to 3D systems.

Equilibrium magnetization configurations in a static field may be determined using iterative free-energy-gradient-based methods. These methods are very efficient when only one local free-energy minimum exists. However, when the system configuration is close to a bifurcation point, i.e., when it may evolve into several possible states, symmetry breaking in the absence of an external perturbation cannot be correctly described. To bypass the bifurcation problem we adopted the method which consists in integrating the dynamic Landau-Lifshitz-Gilbert equation (the LLG equation hereafter):

$$\frac{d\mathbf{m}}{dt} = -\mathbf{m}\times\mathbf{H}_{\mathrm{eff}}(\mathbf{t}), \tag{16}$$

with

$$\mathbf{H}_{\mathrm{eff}}(\mathbf{t}) = \mathbf{H}(\mathbf{t}) + \alpha\mathbf{m}(\mathbf{t})\times\mathbf{H}(\mathbf{t}), \tag{17}$$

where $\mathbf{t}$ is an evolution variable, α is the Gilbert damping constant and $\mathbf{H}(\mathbf{t})$ denotes the field derived from the magnetic energy $\mathbf{F}\{\mathbf{m}(\mathbf{r})\}$ such as

$$\delta F = -\mu_0 M_{\mathrm{s}}\int_V d^3r\,\delta\mathbf{m}\cdot\mathbf{H}(\mathbf{t}). \tag{18}$$

At equilibrium, the torque created by the effective field on the magnetization vector must vanish at any point of the system. This condition is automatically fulfilled in the bulk of the system when Equation (16) is solved. Equation (18) applied near the system surface gives rise to the so-called homogeneous Brown condition, expressed as $\partial_{\mathbf{n}}\mathbf{m}=0$, assuming no surface anisotropy contribution.

Classical numerical methods[16] were used to solve Eq. (16). Both equilibrium and transient magnetization configurations were obtained. The evolution of $\mathbf{m}$, governed by Eq. (13), may be described by the explicit formulation

$$\mathbf{m}(\mathbf{t}+\delta\mathbf{t}) = \mathbf{m}(\mathbf{t})\cos[\mathbf{H}_{\mathrm{eff}}(\mathbf{t})\,\delta\mathbf{t}] + \frac{\sin[\mathbf{H}_{\mathrm{eff}}(\mathbf{t})\quad\delta\mathbf{t}]}{\mathbf{H}_{\mathrm{eff}}(\mathbf{t})}[\mathbf{H}_{\mathrm{eff}}(\mathbf{t})\times\mathbf{m}(\mathbf{t})] \tag{19}$$

$$+\{1-\cos[H_{\mathrm{eff}}(t)\,\delta t]\}\frac{\mathbf{H}_{\mathrm{eff}}(\mathbf{t})\cdot\mathbf{m}(\mathbf{t})}{H^2_{\mathrm{eff}}(t)}\mathbf{H}_{\mathrm{eff}}(\mathbf{t}). \tag{20}$$

This development allows the numerical integration of the LLG equation to be obtained correctly in the limit of a weak t dependence of the effective field $\mathbf{H}_{\mathrm{eff}}$. Otherwise, numerical instabilities may be encountered, which means that outside a certain stability domain the explicit formulation given above does not converge to the true solution of the LLG equations. A stability criterion may be determined in the case of ferromagnetic systems were the evolution of the system is mainly governed by exchange interactions. Let us consider, for example, a chain of spins located on an x axis and directed along z. When the system is weakly perturbed, each magnetization vector $\mathbf{m}(\mathbf{r})$ remains aligned essentially along the Oz axis, so that its components (u,v) in the (x,y) plane are much smaller than 1. Within this limit, the LLG equations may be solved by introducing the complex notation $z = u+iv$,

$$\frac{dz}{dt} = D(\alpha - i)\nabla^2 z, \tag{21}$$

where $D = 2A/\mu_0 M_s$. The Von Neumann stability analysis shows that a time step upper limit exists above which an unstable evolution of the system may appear. This upper limit is given by

$$\delta t_{\mathrm{lim}}^{1\mathrm{D}} = \frac{a_x^2}{8A} \mu_0 M_s \frac{2\alpha}{1+\alpha^2}. \tag{22}$$

A similar analysis may be performed for 3D systems, and leads to the same value, substituting $1/(a_x^2 + a_y^2 + a_z^2)$ for $1/a_x^2$. In our calculation, we took $\alpha = 1$, the maximum value of $\delta t_{\mathrm{lim}}^{3\mathrm{D}}$ then obtained corresponding to the computational time being reduced to its minimum. A more detailed discussion about stability criteria taking into account the anisotropy of the material will be published elsewhere.[17]

A key issue in micromagnetics is the choice of the grid spacing. The calculation outputs are all the more accurate as the grid spacing is small, but this has to be paid by a large computing time. It is usually assumed that the grid spacing has to be taken much smaller than all relevant magnetic lengths in the system: the exchange length $\lambda_{\mathrm{ex}} = \pi \sqrt{A/\mu_0 M_s^2}$ and the wall width, which corresponds to a Néel wall width λ_n in the case of thin films. The evaluation of λ_n generally requires numerical calculations because exchange, anisotropy, and magnetostatic energies are relevant. For ultrathin films with inplane magnetization, the magnetostatic influence is short ranged (see the discussion in Sec. V), so that essentially exchange and anisotropy energies are relevant, the minimization of whose yields $\lambda_n = \pi\sqrt{A/K}$ (for a first order anisotropy), as in the case of a Bloch wall. The difference lies in the fact that the magnetization rotates *parallel* to the wall plane for a Bloch wall and *perpendicular* to it for a Néel wall. As a conclusion, even if the micromagnetic configuration is very different in each situations, $\lambda_n \approx \lambda_b$ for ultrathin films. In the sample presented here, $\lambda_{\mathrm{ex}} \approx 80$ Å and $\lambda_n \approx 1000$ Å at 150 K.

The exchange length λ_{ex} results from the competition between magnetostatic and exchange energies. In the present case, where surface poles are located on the particle edges only, λ_{ex} may be relevant only in the close vicinity of an edge. In the bulk of a particle the magnetization-variation characteristic length is the Néel wall width λ_n. Nucleation volumes have to grow up to dimensions comparable to λ_n to expand into the particle, and thus to reverse its magnetization state. Using a grid with a lateral extension a larger than λ_{ex} but smaller than λ_n may lead to errors near the edges, but should well describe the bulk behavior of the particle. For the present numerical calculation, where we are mainly interested in the shape of the reversal loop and not in the accurate magnetization configuration in the vicinity of the edges, λ_n can be considered as the characteristic length of the system. Thus we chose $a = 125$ Å and $a_z = 30$ Å. However, in order to check the argument given above about the irrelevance of λ_{ex} in the present case, we once performed a calculation with $a = 50$ Å and $a_z = 30$ Å. The $m(h)$ curve and the value of the coercive field were the same than with $a = 125$ Å and $a_z = 30$ Å within a 0.5% accuracy. More generally, the same argument stands for all the anisotropy sources (discussed below) originating in or relevant to the vicinity of the particle edges only: edge interface anisotropy, 3D formulation for anisotropies, roughness over distances much smaller than λ_n, moderate rounding of the corners, etc.

The grid extension outside the magnetized particle was chosen to be 90 Å along z, and 1250 Å along x and y. We used a one-step renormalization for the evaluation of ϕ, which proved to be the best optimization between gains due to the grid expansion and losses due to the grid coarsening during a renormalization step.

The anisotropy in thin films comes from volume and surface contributions. The former appears in Eq. (10), whereas the latter should be taken into account by modifying the Brown condition. In the present case, however, the particle's thickness (60 Å) is negligible as compared to the Néel wall width ($\lambda_n \sim 1000$ Å), the magnetization should thus be nearly homogeneous throughout the thickness of the film, so that the interface anisotropy can be renormalized to the volume and taken into account as a volume contribution in Eq. (10). No interface anisotropy coming from the edges of the particles was taken into account, mainly because of a lack of knowledge about its nature (Fe/W or Fe/Cu) and microstructure. However, this approximation should not be too drastic, as explained as follows. (1) As for the out-of-plane contribution (i.e., perpendicular to the film), it is unlikely to overcome the particle shape effect as the former takes effect over the thickness of the film (60 Å) whereas the latter takes effect over the surface of the 5000-Å-wide particle. (2) The case of the in-plane contribution (i.e., in the plane of the film, either perpendicular or parallel to the edge) is more tricky, as it was recently reported that the island edge's contribution to the anisotropy could be non-negligible.[18] We think that this contribution is not so important in our case because the symmetry broken at particle edges (fourfold to twofold) is also broken on the particle Fe/W interface, which was not the case in Ref. 18, so that the edge contribution should remain relatively small. We indeed observed experimentally that hard axis magnetization loops were not very different in the particles than in the continuous film and used the phenomenological anisotropy constants in the calculation (see Sec. III). The magnetization vector in the present case is expected to remain in plane, so that the anisotropy energy in the particle may be described by Eq. (3). However, to check this point, we once performed a single calculation with magnetization free to point out of plane, so that the 3D form of the anisotropy free energy had to be used in the calculations. The magnetoelastic, volume magnetocrystalline, and surface anisotropy contributions are expressed, respectively, as

$$E_{\mathrm{mc}} = K_{\mathrm{cub}}\left(\tfrac{1}{4}\cos^4\theta + \tfrac{1}{4}\sin^4\theta \sin^4\varphi + \sin^4\theta \cos^2\varphi \sin^2\varphi\right. \tag{23}$$

$$\left. - \tfrac{1}{2}\cos^2\theta \sin^2\theta \sin^2\varphi + \cos^2\theta \sin^2\theta \cos^2\varphi\right), \tag{24}$$

$$E_s = \frac{A_s}{t}\sin^2\theta + \frac{A_{s,p}}{t}\sin^2\theta \cos^2\varphi, \tag{25}$$

$$E_{\mathrm{mel}} = \left[(b^{\gamma,2} - b^{\epsilon,2})\sin^2\theta \cos^2\theta - 2b^{\epsilon,2}\cos^2\theta\right]\frac{\epsilon_\parallel - \epsilon_\perp}{2}. \tag{26}$$

K_{cub} is the cubic first-order magnetocrystalline anisotropy constant. A_s and $A_{s,p}$, respectively, are in-plane and out-of-

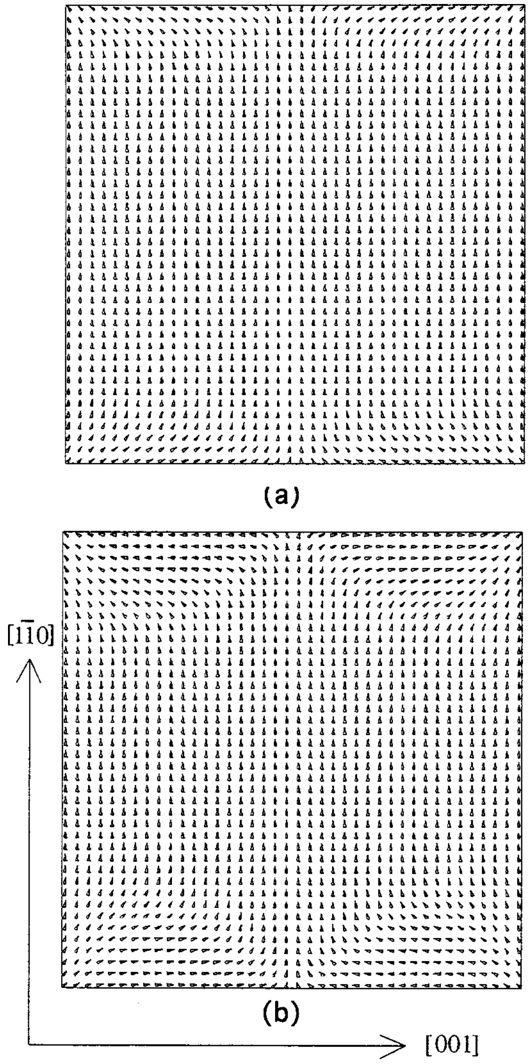

FIG. 10. Simulated static magnetization configurations at zero field (a) and just before h_c (b).

plane first-order surface anisotropy constants.[8] $b^{\gamma,2}$ and $b^{\epsilon,2}$ are magnetoelastic constants, and $\epsilon_\parallel$ and $\epsilon_\perp$ respectively, are the in-plane and out-of-plane strains. As there appeared to be no significant deviation from the results associated with the 2D form of the anisotropy, we used the simpler 2D form of the anisotropy in all calculations. This decreased the calculation time, and partly justifies the above-mentioned approximation about edge-induced anisotropies. In a first approximation the calculation was done for perfectly square particles, using parallelepipedic unit cells with height a_z, and with a square base $(a_x = a_y = a)$.

Static magnetization configurations at different stages of the reversal loop are shown in Fig. 10. In zero field there are four symmetrical regions in the particle, each located on an upper or lower edge of the square, not far from a corner, in which the magnetization deviates significantly from the easy axis direction. In the following we will denote these regions as ''non-saturated (n.s.) volumes.'' Each of these n.s. volumes breaks all the symmetries of the uniaxial-anisotropy cubic particle, but the set of the four n.s. volumes retains all the symmetries of the uniformly magnetized particle. As h approaches h_c, each of the n.s. volumes grows up to a domain with magnetization perpendicular to the field, and of lateral dimensions close to λ_n. This calculated static magnetization configuration clearly illustrates the discussion on coercivity in Sec. II: $h_c \ll h_{SW}$, because the magnetization is not saturated in the nucleation volumes, even before h_c is reached. The simulation yields $\mu_0 h_c = -20$ mT, whereas $\mu_0 h_{SW} = -55$ mT. The coercive field is considerably reduced with respect to $\mu_0 h_{SW}$, due to the nonsaturated initial magnetization configuration in the particles. This calculated value is obtained for a perfect particle, i.e., a large reduction in h_c occurs which is an intrinsic effect associated with the specific shape of the particle.

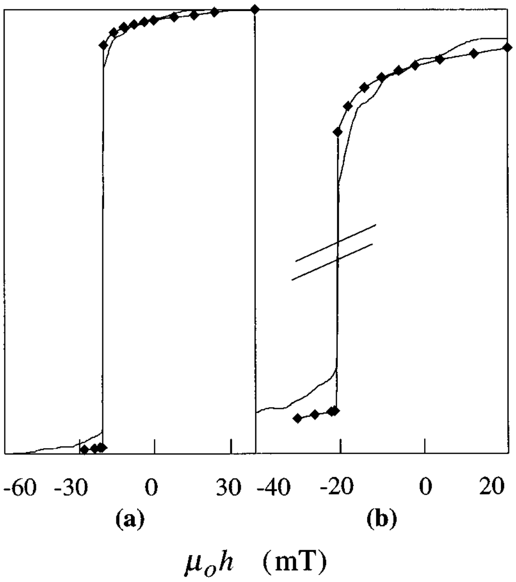

FIG. 11. Mean experimental (line) and simulated (diamonded line) hysteresis loop for a single particle. The experimental loop is superimposed to the simulated one by choosing $\mu_0 h_c = -20$ mT for easier comparison.

Finally we compare the calculated reversal loop to that deduced experimentally by the deconvolution method. The experimental value $\mu_0 h_c = -14$ mT is much closer to the calculated value $\mu_0 h_c = -20$ mT than to $\mu_0 h_{cf} = -4$ mT, the experimental coercive field of the continuous film. It also found that the reversible magnetization variation closely follows the experimental one (Fig. 11). This good agreement between experiments and calculation curves suggests that the actual reversal in the particles corresponds to the mechanism described by the numerical calculation, and not to nucleation at local defects, as is the case in the continuous film.

VI. CONCLUSION

We have optimized a process to obtain nonoxydized W(110)/Fe(110)/W(110) quasi-2D submicron particles with in-plane magnetization using x-ray lithography. The coercive field of the film along the easy axis was increased by 300% by the patterning. This dramatic increase is thought to be the combined consequences of the reduction of the influence of local defects for isolated particles on the one hand, and of the small demagnetizing influence of the one-dimensional surface poles for in-plane magnetization two-dimensional particles on the other hand. The coercive field is therefore expected to remain quite as high for wider particles (as long as the mean defect density in a particle is far smaller than 1), and should tend toward the coherent-rotation coercive field when thickness is progressively reduced toward zero. Further studies are in progress in order to check this point.

We propose a method that allows the determination of the distribution function of coercive fields and of the mean hysteresis loop of a single particle, using macroscopic magnetic measurements over the whole array of particles. The distribution function width is found to be larger than expected from interparticle dipolar contributions and thickness fluctuations only.

We performed careful micromagnetic calculations on ideally square particles by solving the LLG equations and using a renormalization technique. Good agreement was found with all main experimental features of the reversal loop. The magnetization reversal process can be described as the emergence of four symmetric nonsaturated volumes at the edges of the particle, which allows a considerable reduction of the coercive field as compared to the SW coherent-rotation field. This reduction in h_c is an intrinsic phenomena which is independent of any defect sources.

ACKNOWLEDGMENTS

We acknowledge the helpful contributions of B. Pannetier, J. Chaussy, and T. Fournier (CRTBT-CNRS) concerning the etching processes.

---

[1] N. Bardou, B. Bartenlian, C. Chappert, R. Megy, P. Veillet, J. P. Renard, F. Rousseaux, M. F. Ravet, J. P. Jamet, and P. Meyer, J. Appl. Phys. **79**, 5848 (1996).

[2] H. Fritzshe, H. J. Elmers, and U. Gradmann, J. Magn. Magn. Mater. **135**, 343 (1994).

[3] O. Fruchart, J.-P. Nozières, and D. Givord, J. Magn. Magn. Mater **165**, 508 (1997).

[4] F. Rousseaux, Y. Chen, A. M. Haghiri-Gosnet, and H. Launois, Nucl. Instrum. Methods Phys. Res. A **359**, 388 (1995).

[5] F. Rousseaux, D. Decanini, F. Carcenac, E. Cambril, M. F. Ravet, C. Chappert, N. Bardou, B. Bartenlian, and P. Veuillet, J. Vac. Sci. Technol. B **13**, 2787 (1995).

[6] W. Wernsdorfer, E. Bonet Orozco, K. Hasselbach, A. Benoit, B. Barbara, N. Demoncy, A. Loiseau, H. Pascard, and D. Mailly, Phys. Rev. Lett. **78**, 1791 (1997).

[7] M. E. Schabes, J. Magn. Magn. Mater. **95**, 249 (1991).

[8] G. T. Rado, Phys. Rev. B **26**, 295 (1982).

[9] D. Givord and M. F. Rossignol, in *Rare-Earth Iron Permanent Magnets*, edited by J. M. D. Coey (Clarendon, Oxford, 1996), p. 224.

[10] E. C. Stoner and E. P. Wohlfarth, Philos. Trans. R. Soc. London, Ser. A **240**, 599 (1948).

[11] R. M. H. New, R. F. W. White, R. M. Osgood, and K. Babcock (unpublished).

[12] M. Hehn, K. Ounadjela, J. P. Bucher, F. Rousseaux, D. Decanini, B. Bartenlian, and C. Chappert, Science **272**, 1782 (1996).

[13] I. D. Mayergoyz, *Mathematical Models of Hysteresis* (Springer-Verlag, New York, 1991).

[14] Y. Igarashi and M. Kanayama, J. Appl. Phys. **57**, 849 (1985).

[15] W. Wernsdorfer, K. Hasselbach, A. Benoit, G. Cernicchiaro, D. Mailly, B. Barbara, and L. Thomas, J. Magn. Magn. Mater. **151**, 38 (1995).

[16] Y. Nakatani, Y. Uesaka, and N. Hayashi, Jpn. J. Appl. Phys. **28**, 2485 (1989).

[17] B. Kevorkian *et al.* (unpublished).

[18] A. Moschel, R. A. Hyman, A. Zangwill, and M. D. Stiles, Phys. Rev. Lett. **77**, 3653 (1996).